The Role of Fluorine-Functionalized Organic Spacers for Defect Passivation and Low-Dimensional Phase Formation in 3D MAPI Perovskite Solar Cells

Ali Semerci, Javier Urieta-Mora, Sander Driessen, Ali Buyruk, Rik Hooijer, Agustín Molina-Ontoria, Bülent Alkan, Seckin Akin, Mattia Fanetti, Harishankar Balakrishnan, Achim Hartschuh, Shuxia Tao, Nazario Martín, Peter Müller-Buschbaum, Saim Emin, and Tayebeh Ameri**

Widespread application of organic-inorganic halide perovskites (OIHP) still faces a major obstacle in mitigating moisture-induced degradation. Integrating organic spacers, as defect passivation facilitators along with low-dimensional phase (LDP) formation is an effective approach to enhance the efficiency and robustness of 3D methyl ammonium lead iodide (MAPI) in photovoltaics (PV). Here, the formamidinium cation (FA+) employing 3,5-difluorobenzene-1-carboximidamidium iodide (2F), 4-(trifluoromethyl)benzene-1-carboximidamidium iodide (3F), and 2,3,4,5,6-pentafluorobenzene-1-carboximidamidium iodide (5F) organic spacers as passivation layer in 3D/LDP OIHP solar cells is utilized. Fluorine atom position and quantity in organic spacers change the optoelectronic characteristics of the perovskites, enhancing hydrophobicity, facilitating LDP formation, and augmenting dipole moments, thereby facilitating charge separation processes. PV performance analysis reveals that 3F-treated 3D/LDP devices achieve the highest efficiency of 19.22%. Experimental results and density functional theory (DFT) studies attribute the higher performance of 3F-modified devices to effective LDP formation, enhanced passivation of defect states at perovskite surfaces and grain boundaries, the highest dipole moment and lowest band gap among the evaluated spacers. The stability tests show that, after 1000 h, 3F- and 5F-modified 3D/LDP OIHP devices retain over 85% of their initial efficiency. This research opens novel avenues for designing appropriate organic spacers to attenuate defects in 3D/LDP PV devices.

1. Introduction

In recent years, organic-inorganic 3D halide perovskites (OIHP) have gained prominence as a top contender in advanced thin film PV technology, demonstrating significant advancements.[1–3] The power conversion efficiency (PCE) of 3D OIHP has risen considerably, increasing from 3.8% to 25.73% (certified).[4–5] OIHP is a potential material for low-cost PV due to its unique features, which include a high absorption coefficient, low binding energy, long charge carrier diffusion length, high carrier mobility, and adjustable bandgap.[6–10] The industrial use of 3D perovskite solar cells (PSCs) continues to be hampered by their poor intrinsic stability against moisture and temperature under ambient operating conditions, despite the significant progress that has been made in PCE.[10–14]

The film quality of perovskite material is an important factor in the high performance and stability of PSCs. When perovskite films are produced using the conventional solution technique, there is a high probability that defects will occur at the surfaces and grain boundaries.[15,16]

A. Semerci, A. Buyruk, R. Hooijer, H. Balakrishnan, A. Hartschuh, T. Ameri
Department of Chemistry and Center for NanoScience (CeNS)
Ludwig-Maximilians-Universität München
Butenandtstrasse 5–13 (E), 81377 Munich, Germany
E-mail: tam@tf.uni-kiel.de

The ORCID identification number(s) for the author(s) of this article can be found under https://doi.org/10.1002/adfm.202423109

DOI: 10.1002/adfm.202423109

A. Semerci
Faculty of Science, Department of Energy Science and Technologies
Türk-Alman University
2nd Floor Şahinkaya Street No:94, Beykoz, İstanbul 34820, Turkey

J. Urieta-Mora, N. Martín
IMDEA-Nanociencia, C/ Faraday, 9
Campus de Cantoblanco
Madrid 28049, Spain

J. Urieta-Mora, A. Molina-Ontoria, N. Martín
Department of Organic Chemistry, Faculty of Chemistry
Complutense University of Madrid
Avenida Complutense s/n, Madrid 28040, Spain

It is common knowledge that the defect sites that are present at either the surface or the grain boundaries are the typical starting point for the degradation of perovskite. Therefore, the presence of grain boundaries makes it easier for moisture and oxygen from the surrounding environment to penetrate into perovskite films, which in turn speeds up the process of perovskite decomposition.[17–19] Previous studies have shown that the instability of PSCs is mainly caused by trapped charges. Organic cations such as $CH_3NH_3^+$ (MA^+) or $NH_2CH = NH_2^+$ (FA^+) have limited freedom for ion migration at higher temperatures, thus contributing to the instability of 3D perovskite frameworks. The defects result in decreased efficiency by affecting charge carrier dynamics due to an imbalanced distribution of charges and the unstable nature of the PSCs.[20–24] Defects arise when perovskite sheet crystallizes in-situ, leading to non-radiative recombination losses in device operations. Common point defects with low formation energies in MAPI thin films include uncoordinated Pb^{2+}, uncoordinated halide ions, Pb clusters, and Pb-I antisite defects. Hence, it is essential to eliminate imperfections in perovskite films to enhance stability without compromising the efficiency of PSCs.[25–31]

Low-dimensional PSCs have drawn increasing interest over the past couple of years.[32] A commonly employed approach to reduce non-radiative recombination in 3D MAPI perovskites is to either treat surface defects with properly functionalized molecules or introduce low-dimensional perovskites (1D or 2D).[33–36] A wide range of substances, including Lewis bases, and acids, metal cations, metal anions, and alkylammonium halogenides, have been employed as passivation agents to mitigate the structural defects in perovskites.[37] Moreover, when introduced into 3D perovskite frameworks, LDPs act as passivating agents, minimizing the influence of defects. Additionally, the LDPs act as heterojunctions, enhancing the fluorescence lifetimes inside the perovskite framework.[38] In comparison to their 3D counterparts, the presence of large organic spacer cations greatly increases the moisture resistance of LDP structures. However, the LDP PSCs typically exhibit a comparatively diminished PCE due to the limited charge transport capabilities, high exciton binding energies, and wider band gap, acting as insulators.[39,40]

Mixed-dimensional perovskites (3D/LDP) are considered a promising strategy for PSCs. Thus, the advantages of two different perovskite derivatives are combined. The 3D perovskite controls optical absorption and charge transport qualities, while a thin hydrophobic LDP seals defects on the surface and protects the 3D perovskite from moisture. The LDP also aligns the energy bands and regulates the film quality of the 3D perovskite structure.[41,42] For example, advancements in 3D/LDP PSCs have mostly focused on modifying the optoelectronic characteristics of 2D Ruddlesden-Popper phases by altering the organic spacers.[43] LDP often exhibit a significantly higher exciton binding energy due to their robust quantum and dielectric confinement.[44] To decrease the dielectric confinement leading to low charge transfer in perovskite devices, an effective strategy is to create organic spacers with a high dielectric constant through enhancing molecular dipole moments. Functional groups with high electronegativity are utilized to create an appropriate organic spacer for this purpose. Fluorine (F) as the most electronegative element is often used as a functional unit to design organic spacers to raise the dipole moment and dielectric constant.[45–48] Wie et al. were among the pioneers who introduced F atoms into lead-based PSCs.[49] Following that, organic spacers 4-Trifluoromethyl-phenethylammonium (CF_3-PEA), 4-(trifluoromethyl)benzylammonium iodide (TFMBAI), 4-(trifluoromethyl) benzylamine (4TFBZA), 3-fluoro-benzyl ammonium iodide (3FBAI), and 2-[4-phenyl]ethanamine were utilized in 2D and 3D/2D PSCs.[50–55] The fluorinated substances are reported to improve device performance. In general, organic spacers that incorporate amine (-NH_2) functional groups are extensively employed to supplement the 3D perovskite film with an LDP protective layer.[56] Conversely, when compared to the amine groups, the formamidinium (FA) functional group interacts more strongly with Pb-I octahedrons and demonstrates superior charge transport capability.[57,58] To fabricate an LDP perovskite structure, organic spacers containing FA group (e.g., benzamidine (PhFA), 2-thiopheneformamidinium (ThFA), and para-fluorobenzamidine (p-FPhFA)) have been the subject of very few investigations.[59,60] Given this knowledge, it is clear that a systematic study is required for building organic spacers to obtain insight into the mix-dimensional perovskite formation, which influences the passivation mechanism and efficiency of PSCs.

In this study, 3,5-difluorobenzene-1-carboximidamidium iodide, 4-(trifluoromethyl)benzene-1-carboximidamidium iodide, and 2,3,4,5,6-pentafluorobenzene-1-carboximidamidium iodide from the same family containing F atoms and FA functional groups, referred to as 2F, 3F, and 5F, were utilized to create an LDP on 3D MAPI PSCs. The acronyms 2F, 3F, and 5F represent the number of F atoms contained in the molecules. The study examined how the dipole moment of organic spacers affects the

---

S. Driessen, S. Tao
Materials Simulation and Modelling, Department of Applied Physics
Eindhoven University of Technology
Eindhoven 5600 MB, The Netherlands

B. Alkan
Department of Metallurgical and Materials Engineering
Hitit University
Corum 19030, Turkey

S. Akin
Department of Metallurgical and Materials Engineering
Necmettin Erbakan University
Konya 42090, Turkey

M. Fanetti, S. Emin
Materials Research Laboratory
University of Nova Gorica
Vipavska 13c, Ajdovščina 5270, Slovenia
E-mail: saim.emin@ung.si

P. Müller-Buschbaum
TUM School of Natural Sciences, Department of Physics
Chair for Functional Materials
Technical University of Munich
James-Franck-Str. 1, 85748 Garching, Germany

T. Ameri
Chair for Composite Materials, Department of Materials Science
Faculty of Engineering
Christian-Albrechts-Universität zu Kiel
Kaiserstrasse 2, 24143 Kiel, Germany

T. Ameri
Kiel Nano, Surface and Interface Science KiNSIS
Kiel University
Christian-Albrechts-Platz 4, D-24118 Kiel, Germany

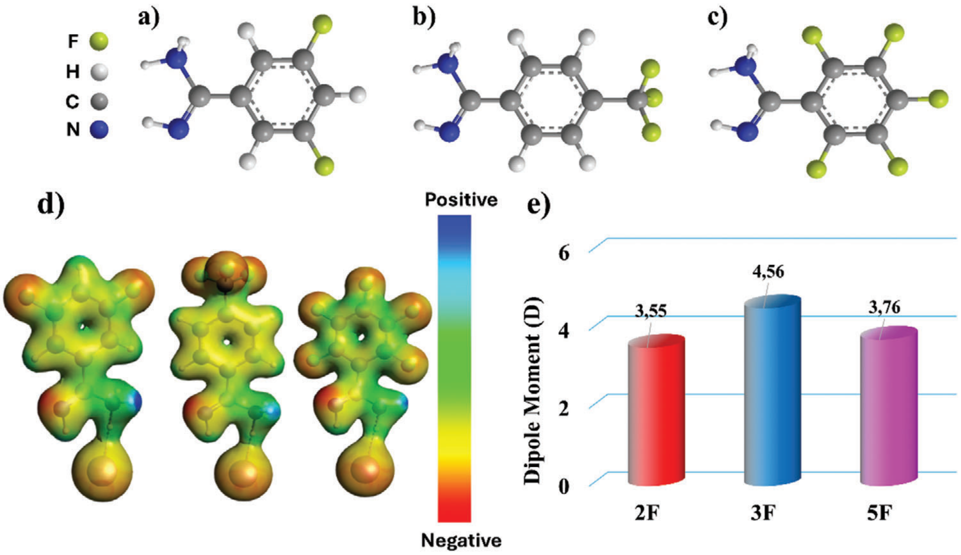

Figure 1. a–c) Molecular structure of 2F, 3F, 5F organic spacer, respectively. d) Electrostatic potential (ESP) analysis of the xF-organic spacers ($x = 2, 3, 5$). The color bar indicates the self-consistent field coulomb potential (SCF-Coulpot): negative (red) and positive (blue); e) Calculated molecular dipole moments of 2F, 3F and 5F molecules.

performance of PSCs by the passivation of trap states. Cathodoluminescence (CL) investigations, a powerful technique, also reveal certain aspects of LDP generation on perovskite surfaces. High-resolution transmission electron microscopy (HR-TEM) observations provided additional evidence for the existence of LDP, as seen by the significant lattice spacings obtained. To gain more insight into the effect of these fluorinated spacers, we conduct DFT calculations to examine the interactions between the passivation species and the 3D MAPI surface. The stability investigation involves calculating the binding energy (E_b) of fluorinated organic molecules on the Pb-I terminated perovskite surfaces. The DFT calculations show that the bonding strength between fluorinated molecules and MAPI surfaces is significantly increased. The strongest binding is found for the 3F spacer, due to its largest dipole moment. This enhancement plays a major role in the passivation of the perovskite surface.

2. Results and Discussion

Figure 1a–c depicts the molecular structure of the organic spacers 2F, 3F, and 5F utilized in this study. Nuclear magnetic resonance (^{1}H-, ^{19}F-NMR) and mass spectroscopy were used to characterize the compounds (Figures S1–S4, Supporting Information). All three organic spacers possess FA and F as functional groups, which are either directly or indirectly connected to a benzene ring. Previous studies have shown that fluorinated organic spacer cations with high polarity can increase the dielectric constant.[61] This results in a reduction of the coulomb force between the exciton's electron and hole pair, thereby promoting effective charge separation. Research indicates that the use of fluorinated spacers enhances several characteristics of low-dimensional perovskites, mostly due to their tunable dipole moments.[62]

Dipole moments of organic spacers were calculated to comprehend how the number of F atoms and their position in the aromatic ring affect the dipole moment as illustrated in Figure 1d,e. The respective dipole moments of molecules 2F, 5F, and 3F are calculated in DFT calculations, and values of 3.55, 3.76, and 4.56 D, were obtained, respectively. The differences in dipole moments have a significant impact on the quality of the modified perovskite films and the performance of the devices.

The 3D/LDP PSCs device was fabricated by spin-coating organic spacers to form an LDP perovskite structure on 3D MAPI films. Scanning electron microscopy (SEM) studies were conducted to assess the morphology of 3D control with 5% of excess lead iodide (PbI_2), 2F, 3F, and 5F-3D/LDP MAPI perovskite films. The top-view SEM images in **Figure** 2a–d demonstrate that the active MAPI layers fully coat the substrate surface. Additionally, there is excess PbI_2 along grain boundaries, which appear in the form of small particles (yellow circles) in the 3D control (Figure 2a).

The crystal grains of the 3D control with clear boundaries vary from several hundred nanometers to a micron range size as depicted in Figure 2a. On the other side, the modified perovskite films display less obvious grain boundaries, as shown in Figure 2b–d, suggesting the occurrence of surface passivation.[52] The size of the grains remains similar when compared to the 3D control film. A small-size conglomeration was found on the surface of 2F-treated films as presented in Figure 2b. Upon analyzing the perovskite phase treated with 3F, one can observe larger and more clearly defined conglomerated formations along the grain boundaries as shown in Figure 2c. It demonstrates that 5F follows a similar pattern in Figure 2d. Moreover, the excess PbI_2 situated at the interfaces of the perovskite grains undergoes partial consumption when treated with 2F, while experiencing a more substantial consumption in the case of perovskite treated with 3F and 5F (as shown below in CL part). The FA^+ functional group of these spacers is expected to react with uncoordinated surface Pb atoms.[58] The conglomerations can influence the charge transfer across the grains due to changes in the interfacial dipole caused by this interaction.[63] SEM analysis was

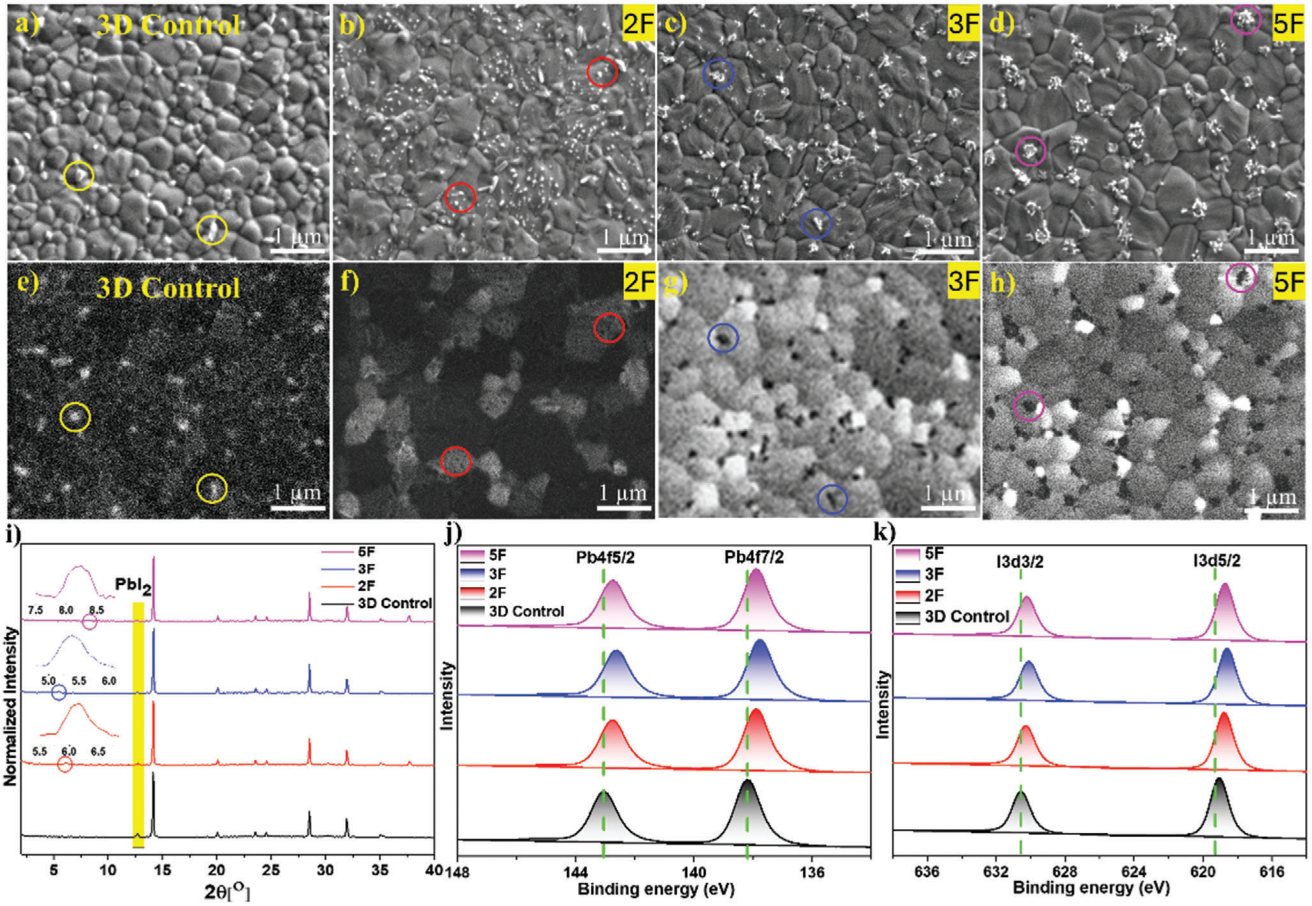

Figure 2. SEM images of 3D MAPI control film, 2F-3D/LDP, 3F-3D/LDP, and 5F-3D/LDP MAPI perovskite films were recorded using a–d) SED and e–h) CL detectors. i) XRD patterns and j) Pb 4f core level, k) 3d core level XPS spectra of 3D MAPI control film, 2F-3D/LDP, 3F-3D/LDP, and 5F-3D/LDP perovskite films.

also performed on perovskite film surfaces treated with various concentrations of corresponding organic spacers (Figure S5a–c, Supporting Information). SEM images captured with a backscattered electron detector (BED) unveil the presence of distinct phases exhibiting different contrast (Figure S6a–d, Supporting Information). Structures with a brighter color are smaller in size compared to the MAPI grains, primarily appearing between the grains as nanoparticles with irregular shapes. The brighter structures observed at the grain boundaries in the 3D control sample, which includes excess PbI_2 (5%), are attributable to PbI_2. In the treated samples, the alterations in shape, size, and distribution density of these agglomerates indicate that they are not the same excess PbI_2 particles observed in the 3D control film (Figure S6b–d, Supporting Information). The hypothesis is that, in the sample exposed to 2F and 3F, the concentration of PbI_2 diminishes, allowing for the emergence of LDP. In contrast, the 5F passivated sample undergoes complete conversion of PbI_2, resulting in the formation of LDP on the surface of MAPI grains. Additionally, small spots are observed on the MAPI grains, especially in the 2F- and 3F-treated films. In the case of the 5F-treated sample, there are fewer tiny formations, and most of the agglomerates are situated between the MAPI grains. However, the analysis with backscattered electrons cannot unambiguously distinguish between PbI_2 and LDP phases.

CL has proven to be an effective tool for studying the recombination behavior of charge carriers in PV materials, with submicrometer spatial resolution. Moreover, for highly emitting materials (such as MAPI), CL can be useful in distinguishing different phases, when X-ray microanalysis or backscattered electron imaging encounter unfavorable conditions (e.g., materials very sensitive to irradiations). Xiao et al. thoroughly investigated the effect of accelerating voltage and incident electron beam current on the emission parameters of MAPI perovskite films.[64] Their extensive research dives into the changes in emission intensity and spectrum caused by various e-beam excitation settings. A comparison of MAPI emission spectra at various accelerating voltage and beam current settings revealed unique influences on emission properties with time and found that irradiation with low beam energy (such as 2 KeV) at low beam current (<4 nA) are suitable to detect a clear signal without degradation of the sample. We analyzed the surface of specimens with 2 KeV beam energy and ≈0.06 nA beam current. In these conditions, the sample was not visibly degrading, and the CL signal was high enough for analysis. The CL intensity measurement of solution-cast MAPI films developed on ITO-coated glass slides with a SnO_2 layer (≈40 nm) on top of the ITO is shown in Figure 2e. The most intense emission is localized at the PbI_2 grains (two of them indicated with yellow circles in Figure 2e). We observed that the intensity of the different features is subject to a time-dependent process (Figure S7, Supporting Information). At the beginning (i.e., after minimum exposition to e-beam) the most intense emission come from the MAPI grains (Figure S7b, Supporting Information), and in many cases there is an intensity difference between the grains (see also Figure 2f). This indicates that different grains have varied nonradiative recombination rates near the film surface. We hypothesize that the intensity variation can be attributed to different concentrations of surface defects among distinct grains. Longer exposure results in a decrease in perovskite CL intensity, whereas the PbI_2 grains preserve a pronounced CL emission (Figure S7c–e, Supporting Information). In treated perovskite films, there are also darker spots exhibiting much lower (or none) emission as shown in Figure 2f–h (some of them indicated by circles). The appearance of darker spots in the treated films support the disappearance of PbI_2 and validate the formation of a new phase that could be assigned to LDP. In the SEM image captured with a SED detector (Figure 2a–d), these formations appear white. The average size of these structures in the 2F-treated perovskite is less than 100 nm, while the LDP agglomerates in the 3F and 5F typically range between 100 and 300 nm.

Utilizing an atomic force microscope (AFM), the passivated perovskite films were further investigated for changes in their surface roughness. The root mean square (RMS) roughness of the 3D control film is determined to be 10.7 nm. On the other hand, after the treatment the 2F, 3F, and 5F perovskite thin films show RMS values of 7.6, 7.2, and 7.7 nm, respectively (Figure S8, Supporting Information). The lower RMS values are favorable for the deposition of hole transport material (HTM). In addition, the decreased surface roughness of the mixed 3D/LDP film can be accepted to have a positive impact on charge carrier transport resulting in an enhanced performance of derived PSCs.

X-ray diffraction (XRD) was used to analyze the crystallinity of 3D control, and 3D/LDP perovskite films as shown in Figure 2i. The primary XRD peaks of the 3D control are observed at 14.19° and 28.50° 2θ, corresponding to the (110) and (220) planes of MAPI, respectively.[36]

The diffraction peak corresponding to excess PbI_2 was noted at 12.7°. This peak exhibited a decrease in the 2F, 3F, and 5F-treated perovskite films compared to the 3D control, suggesting the conversion of excess PbI_2 to LDP. So that, extra peaks are observed at low 2θ angles of 6.1, 5.4, and 8.2° in the XRD pattern of the 3D/LDP perovskite films treated with 2F, 3F, and 5F, respectively. It was determined that these new signals did not originate from the corresponding organic spacers, as evidenced by the comparison with the XRD analysis of pure organic spacers (Figure S9, Supporting Information). Therefore, the extra peaks are associated with the combined new phases on the 3D perovskite surface as illustrated in Figure 2b–d. The weak reflections at the low 2θ angle (<10°) suggest the presence of LDP formed during annealing, as reported in prior research.[52,65]

X-ray photoelectron spectroscopy (XPS) investigation was conducted to study the surface composition of the treated perovskite films. The passivated samples were found to have the F element from the corresponding organic spacers. The distinct photoemission peak of F atom in core level F1s was detected in the treated perovskite films (Figure S10, Supporting Information). The binding energies of the Pb $4f_{5/2}$ and Pb $4f_{7/2}$ orbitals in the 3D control perovskite, at 143.0 and 138.2 eV are associated with the Pb^{+2}, as illustrated in Figure 2j. The binding energies of $I3d_{3/2}$ and $I3d_{5/2}$ in the pure perovskite are 630.6 and 619.1 eV, respectively, as shown in Figure 2k. In all treated films with the 2F, 3F and 5F organic spacers, both peaks of Pb and I shifted toward lower binding energy compared to the 3D control film (Table S1, Supporting Information). These downward shifts in binding energies suggest that the corresponding organic spacers interact with the uncoordinated Pb^{2+} ions and iodine atoms.[66] In addition, the downward shift in binding energy indicates that LDP facilitates charge transfer in the perovskite structure because the core level signals in the treated films are located closer to the Fermi level.[16,67] The most notable decrease in binding energies within the Pb4f and I3d spectra was observed in the perovskite film treated with 3F, as compared to those treated with 2F and 5F. This suggests that ($-NH_3$) in the 3F perovskite film may be in closer proximity to the $[PbX_6]^{4-}$ octahedron because of enhanced hydrogen bond interactions caused by the electron-withdrawing impact of X-positioned F atoms.[68]

Nuclear magnetic resonance (^{1}H-NMR) was employed to verify NH−I hydrogen-bonding interactions between organic spacers and inorganic lead iodide species (e.g., $[PbI_4(H_2O)_2]^{2-}$ or $[PbI_6]^{4-}$]) (Figure S11, Supporting Information). To indirectly support this observation, ^{1}H-NMR analysis was performed by mixing 3F molecule, containing $-CF_3$ group, with PbI_2, the building block of $[PbI_6]^{4-}$ octahedral in the 3D perovskite crystal. When the spacer and PbI_2 are combined, the protons of the formamidinium $-NH_2$ group in the organic cation that interact with PbI_2 experience a shift toward higher magnetic field values (shielding effect) compared to the ^{1}H-NMR spectrum of the pure 3F molecule. This indirectly indicates that the organic cation interacts with PbI_2 via the FA^+ cation end.[69]

Grazing incidence wide-angle X-ray scattering (GIWAXS) was employed to assess the orientation of perovskite crystallites to the substrate in both the 3D control film and the treated perovskite film with 2F, 3F, and 5F organic spacers. The 3D reference material shows a random orientation, which can be seen through the diffraction rings displayed in **Figure 3**a.[70] The reflection at the azimuthal angle near 0°, beneath the first reflection ring related to 3D MAPI, corresponds to the (001) plane of PbI_2. 3D Control MAPI thin films commonly have an excess of PbI_2 due to surface deterioration of the perovskite layer and the excessive usage of PbI_2 in the perovskite precursor solution.[71] All other materials show similar reflections and random orientation for the 3D MAPI phase. In the 2F and 3F samples, the intensity of the PbI_2 reflections is reduced whereas it is not observable anymore for 5F as shown in Figure 3b–d, demonstrating the partial (2F and 3F) and complete (5F) consumption of the excess PbI_2. Furthermore, additional reflections in the low q region, below the first 3D MAPI reflection ring, can be observed for all three treated materials. For comparison with the XRD and TEM results, a pseudo 2 Theta plot of the low q scattering region is given (Figure S12, Supporting Information).

While the origin of these low-angle reflections was shown not to originate from the pure organic spacer materials, we cannot assign them unambiguously to a solved structure. Nonetheless, the

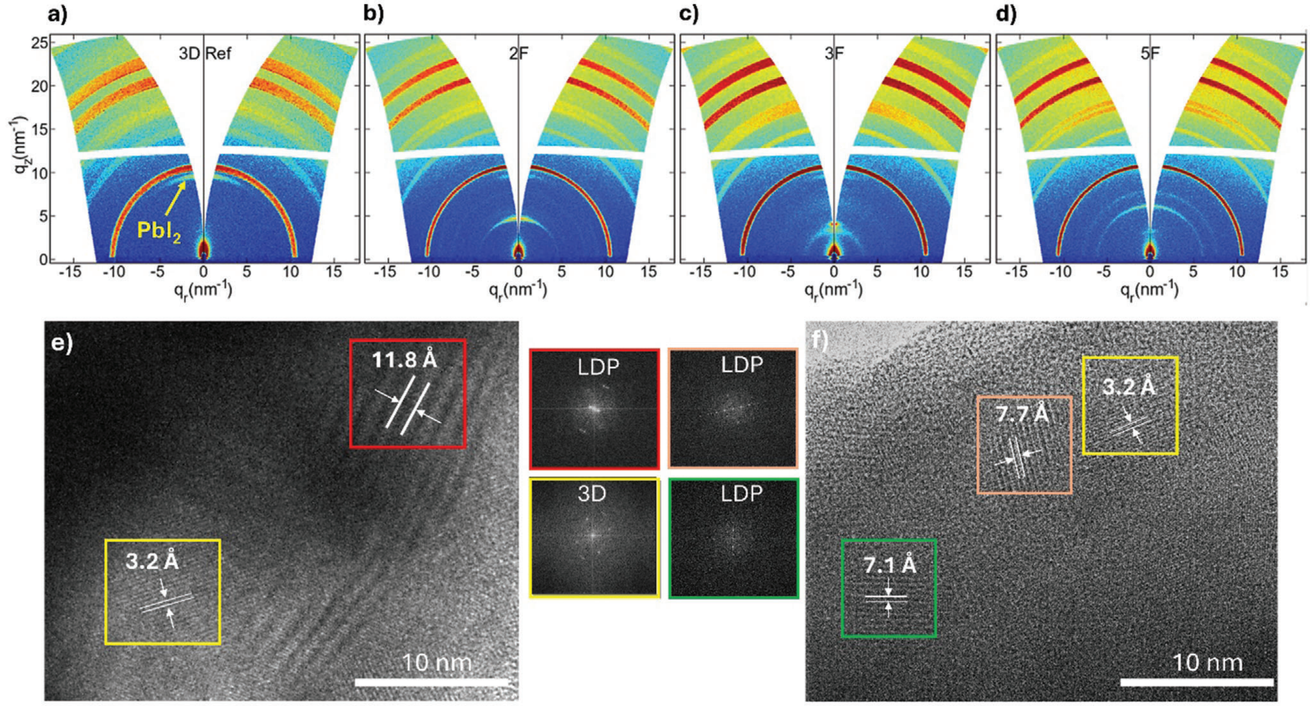

Figure 3. GIWAXS data of a) 3D control MAPI (with +5% excess PbI_2), b) 2F- 3D/LDP, c) 3F- 3D/LDP, d) 5F-3D/LDP perovskite films. e,f) TEM images of 3D/LDP perovskite film treated with 3F and corresponding fast Fourier transforms (FFT) taken from the marked areas.

large unit cell parameters required for the low q region scattering point toward the formation of low-dimensional phases on the surface of the 3D MAPI thin film. The lattice planes of the observed reflections of these LDPs are predominantly oriented parallel to the substrate, as seen by the reflections being located around the azimuthal angle of 0° as shown in Figure 3b–d. Lastly, for 3F the different orientation profiles of the additional reflections, i.e., a broad reflection ring at $q_r = 3.37$ nm^{-1} (4.76° 2θ) and a sharp reflection at $q_r = 4.08$ nm^{-1} (5.72° 2θ) could point to more than one new phase being present.

HR-TEM studies were conducted to clarify the structural features of the 3D/LDP MAPI samples treated with 3F, as depicted in Figure 3e,f. The interplane spacings, which are assessed from the Fast Fourier transform (FFT) images and correlate to the fingerprint of LDP lattice fringes, are visible in the HR-TEM images. The HR-TEM images from certain areas validate the presence of different lattice spacings. The small distance between adjacent crystal planes of 3.2 Å is associated with the (220) diffraction peak of the 3D MAPI tetragonal phase (COD file: 1548467) as shown in Figure 3e.[72] Furthermore, the 3F-treated perovskite films show interplanar *d*- spacing of 7.1, 7.7 and 11.8 Å, which are correlated with the LDP (Figure 3e,f). The observed interplanar d-spacings in HR-TEM are mainly consistent with those of LDP as reported in previous studies.[73,74] Furthermore, The XRD and GIWAXS studies also support the LDP formation within the 3D MAPI structure.[47,75] Assessing the distinctive features of LDP is difficult because of their small numbers and surface localization. Conducting experiments in bulk phase is not useful in clarifying the *n*-values, the number of octahedral layers, or the formula of the LDP phase, as literature that presents *n*-values often pertains to LDPs created from specific stoichiometric ratios of precursors. The quantity of excess PbI_2 at grain boundaries as PbI_2 and the amount of organic spacer reacting with this excess PbI_2 which is observable in XRD pattern, during the spin-coating stage remain unspecified. These results indicate that the final structure we obtained is potentially a mixed-dimensional 3D – low dimensional PSCs.

Our experimental results suggest that the treatment with the fluorine-functionalized organic cations has the potential to improve the efficiency as well as the stability of the MAPI-based solar cells, as a result of LDP formation. We hypothesize that these fluorinated organic spacers passivate also defects on grain boundaries and surfaces of the perovskite film at molecular level, as shown schematically in **Figure** 4a. To gain more insight into the effect of these fluorinated spacers, we conduct DFT calculations to examine the interactions between the used agents and the 3D MAPI surface.

We started with an MA-I terminated perovskite surface and replaced MA cations with xF cations to compare the stability of these modified perovskite surfaces relative to that of 3D MAPI, shown as in Figure 4b. In addition to the xF cations studied experimentally in this work, we also investigated the effect of the NH group in passivating the surface by substituting it with a CH_2 group in the 3F cation. This organic spacer will be referred to as 3FC, amphiphilic 4-(trifluoromethyl)benzylammonium iodide (TFMBAI), which is often reported as a passivation agent previously in literature.[52] To assess the stability of adsorbed molecules, we performed calculations of the binding energy (E_b) for the MA-I ion pair and xF-I structures on the Pb-I terminated perovskite surface. Details of the structural models and the

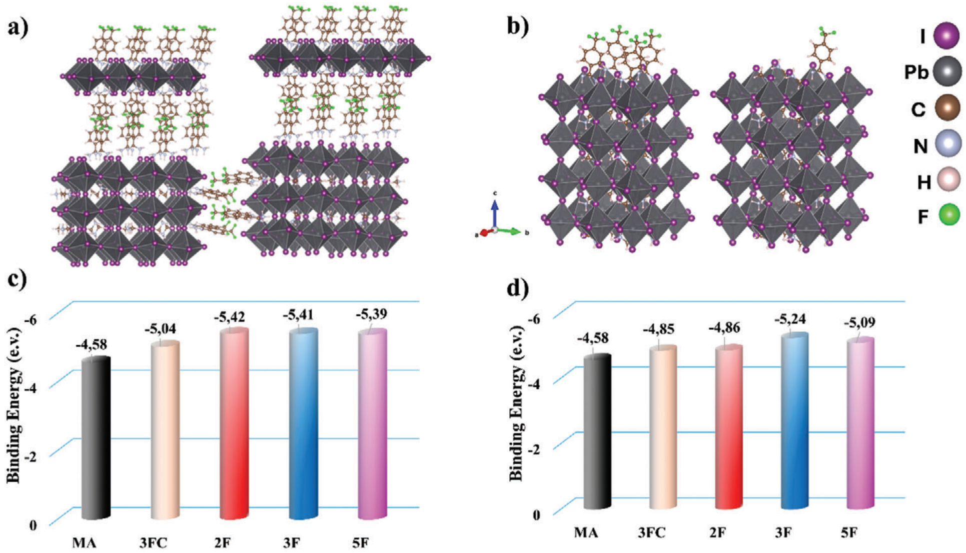

Figure 4. a) A schematic illustration showing how an LDP layer is formed on top of a 3D MAPI, with a perovskite grain boundary passivated by fluorinated organic spacers; b) a diagram showing the perovskite surface with partially fluorinated organic spacers decoration on the right and full organic spacer decoration on the left; c) the binding energy for the perovskite surface fully covered with fluorinated organic cations; d) the binding energy for the perovskite surface with a low coverage of fluorinated organic cations.

calculations can be found in supporting information note for DFT calculations. The calculations were done both for full coverage and low coverage (25%) of the surface with xF organic spacers, as shown in Figure 4b.

The E_b calculation results for the surface fully and partially covered with fluorine-functionalized organic cations are shown in Figure 4c and in Figure 4d respectively. When considering the entire coverage, it is evident that the perovskite surface has a better passivation effect because all the fluorinated organic cations bind to the Pb-I ended surface more firmly than the MA and 3FC organic spacer. Whereas 2F, 3F, and 5F cations have approximately the same Eb, interestingly, a more distinct trend becomes apparent when reducing the coverage. 3F forms the strongest bond with the surface, followed by 5F and 2F as shown in Figure 4d. This trend can be explained by the dipole moments of the fluorinated molecules themselves, which are shown in Figure 1e, where the larger dipole moment of the molecule corresponds to stronger binding to the surface, as a larger dipole moment indicates stronger intermolecular forces leading to more stable molecular interactions. The larger dipole moment of the 3F passivator is ascribed to the position of the fluor atoms on the aromatic ring. For 3F these are all concentrated on the top position on the ring in a trifluoromethyl group, whereas for the other passivators, the fluor atoms are distributed around the aromatic ring. This trend is the same as the one experimentally established for the PCE, confirming the most effective defect passivation effect of the 3F organic spacer. Next to increasing the PCE, passivating dangling bonds on the Pb-I terminated surface leads to increased stability as it minimizes ion migration and defect formation. Also, the stronger passivation, together with the hydrophobic effect of the Fluor atoms, leads to less water infiltration into the crystal, which results in a better long-term stability.

It is important to mention that only very small amounts of the organic cations were used in our experiments. This suggests that it is unlikely for the passivation with organic spacers to fully cover the surface, therefore 3F emerges as the best passivator at low coverage. However, using a large amount of organic cations may also have drawbacks. The insulating character of the organic spacers can be attributed to their predicted band gaps, which exceed 3 eV in according to DFT calculations. Among the organic spacers, 5F has the highest insulation (Figure S13, Supporting Information). Applying high concentration of the organic spacers can therefore hinder the charge transport, since the insulating properties of the fluorinated compounds would be more dominant than the beneficial effect of passivation. We highlight that the passivation effect of these organic cations also improves the stability and performance of the perovskite films and devices, by immobilizing surface halide species and passivating dangling Pb bonds. Here, with the largest surface binding energies, both 3F and 5F significantly improve the long-term stability of the solar cells, with 5F being slightly superior to 3F due to its more hydrophobic nature, as demonstrated in Figure 6a.

UV-vis absorption spectroscopy was used to study the optoelectronic properties of the perovskite films shown in **Figure 5**a. Compared to the 3D MAPI control film, surface-modified 3D/LDP films (≈550 nm thick, Figure S14, Supporting Information) exhibit no notable absorption differences. It indicates that the presence of the LDP phase atop the 3D structure does not cause a significant change in the absorption characteristics of the photoactive film.

As depicted in Figure 5b,c, steady–state photoluminescence (SSPL) and time-resolved photoluminescence decay (TRPL) measurements were performed on the 3D MAPI control and treated 3D/LDP perovskite samples to elucidate the charge recombination processes. The passivated film including 2F shows slightly increased peaks in PL emission, while the pristine perovskite films modified with 3F and 5F demonstrate elevated PL emission peaks, as depicted in Figure 5b.

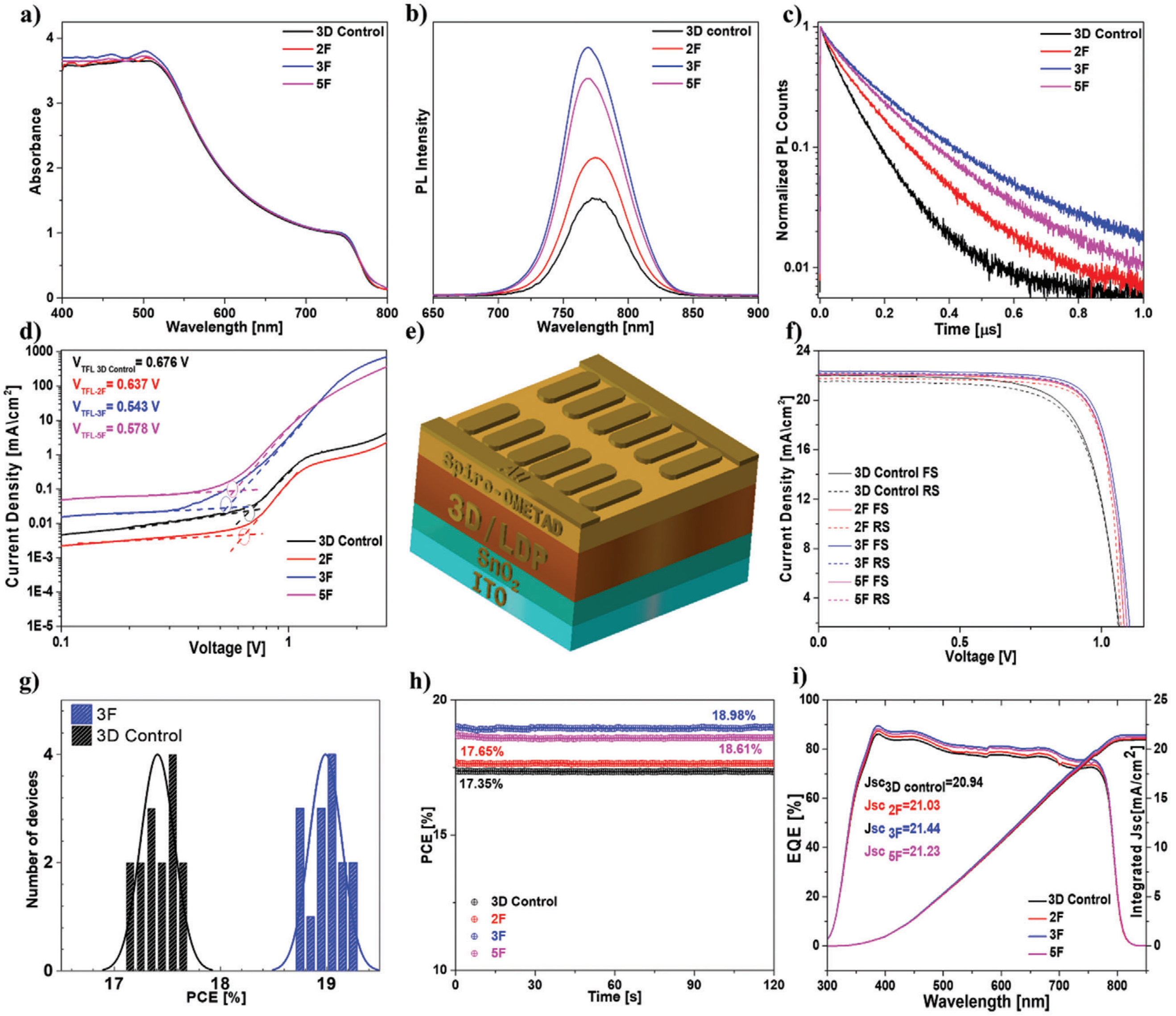

Figure 5. a–c) Absorption, SSPL and TRPL spectra of 3D MAPI control, 2F-3D/LDP, 3F-3D/LDP, and 5F-3D/LDP perovskite films on glass substrate. d) SCLC curves of the Electron only devices for 3D MAPI control, 3D/LDP with 2F, 3F and 5F. e) Device structure of corresponding PSCs reported in this study. f) *J-V* curves of champion devices of 3D control 2F-3D/LDP, 3F-3D/LDP, and 5F-3D/LDP perovskite films respectively. g) Histograms display the distribution of PCE for both the 3D control and 3F-3D/LDP PSCs, for 15 devices each. h) The MPP of PSCs under AM 1.5G light. i) EQE of corresponding devices.

The high PL intensity serves as an indicator of the elimination of defect-related sub-bandgap states in perovskite films.[76] The observed high PL emissions in 3D/LDP perovskite films treated with 3F and 5F can be attributed to ability of the surface defect passivation and LDP phase formation to inhibit non-radiative recombination losses.

Figure 5c illustrates the TRPL decay spectra of the films that were prepared on glass substrates. The TRPL curve was fitted with the biexponential equation (1) given below:

$$y = A_1 exp\left(\frac{-t}{\tau_1}\right) + A_2\ \exp(\frac{-t}{\tau_2}) + y_0 \tag{1}$$

where A_1 and A_2 denote the signal amplitudes. The symbols τ_1 and τ_2 represent, the short and long charge carrier recombination times, respectively. In essence, τ_1 is linked to nonradiative trap-assisted recombination taking place at the perovskite grain boundaries, while τ_2 is associated with bulk carrier recombination, conversely.[67,77]

A compilation of the charge carrier lifetimes of the perovskite films is provided in Table S2 (Supporting Information). The respective τ_1 and τ_2 values in the 3D control film are 50 and 114 ns, respectively. There is no major change in these values in the film treated with 2F. In particular, the 3F-treated 3D/LDP perovskite films exhibit considerably longer τ_1 and τ_2 values than the control sample. The diminished τ_1 value signifies that in the passivated

3F and 5F 3D/LDP, radiative recombination of carriers predominates over trap-assisted nonradiative recombination. Reduced nonradiative recombination is likely linked to a lower defect density, as indicated by the extended lifetimes. This, in turn, promotes charge carrier transport and contributes to an increased open-circuit voltage (V_{oc}).[78]

The trap-state density of the corresponding films was determined using the space-charge-limited current (SCLC) method, which is applicable to electron/hole-only devices. The equation (2) for this calculation is as follows:

$$\mathrm{N_t} = 2\varepsilon\varepsilon_0 \mathrm{V_{TFL}}/\mathrm{qL}^2 \tag{2}$$

where N_t represents the electron or hole trap-state density, ε is the relative dielectric constant of MAPI perovskite (ε = 25), ε_0 represents the vacuum permittivity (8.85×10^{-12} F m^{-1}), V_{TFL} signifies the trap-filled limit voltage, q is the fundamental charge (1.602×10^{-19} C), and L symbolizes the thickness of the perovskite film. For this experiment, electron-only devices were produced and current density-voltage (*J-V*) curves in the dark were collected as shown in Figure 5d.[79] The ohmic region is the linear segment observed in the dark *J-V* curve at low bias voltage. The region characterized by an intermediate bias, where charge carriers occupy traps, is termed the trap-filled region. The region devoid of traps is established at the high-bias voltage. The bias voltage at the inflection points between the ohmic region and the trap-filled region is used to calculate the V_{TLF}. The calculated trap state density of the 3D MAPI control device is 6.17×10^{15} cm^{-3}. The trap-state density of the 3D/LDP perovskite the 2F device is measured at 5.88×10^{15} cm^{-3}. Although the trap density value of the 2F-modified device is lower compared to the 3D control, there is no significant difference. The trap-state densities of 3F and 5F-designed 3D/LDP perovskites were determined to be 4.97×10^{15} cm^{-3} and 5.26×10^{15} cm^{-3}, respectively. The 3D/LDP perovskite device with 3F demonstrates the least trap-state density. This confirms the passivation impact of the fluorinated organic spacers and LDPs, reducing nonradiative recombination and facilitating efficient charge transfer. These factors are pivotal for improving the photovoltaic performance of PSCs.

To assess the impact of the molecular passivation and LDPs on the photovoltaic performance, the *n-i-p* planar (ITO/$\mathrm{SnO_2}$/3D or 3D/LDP/Spiro-OMeTAD/Au) PSCs with 3D MAPI and 3D/LDP mix-dimensional were fabricated as shown in Figure 5e. The results of the best performing devices, as determined through *J–V* characterization at an Air Mass (AM) of 1.5G (1000 W m^2), are depicted in Figure 5f and detailed in Table S3 (Supporting Information). Furthermore, statistical distributions are provided for the photovoltaic parameters to demonstrate the reproducibility of the corresponding devices within acceptable limits as well as to define the best concentration value of LDP film. (Figures S15–S17, Supporting Information).

The 3D MAPI control perovskite device achieved a short-circuit current density (J_{sc}) of 21.99 mA cm^2, an V_{oc} of 1.07 V, and a fill factor (FF) of 74%. Consequently, the best-performing control device attained a PCE of 17.62%. As can be seen in the forward and reverse scans, the 3D control unit suffers from hysteresis. When optimizing with 2F, the efficacy of 3D/LDP PSCs does not increase significantly (17.91%) in comparison to the 3D control. Concerning the 3D/LDP devices treated with 5F, there is an observed improvement in PCE to 18.93% with an increased V_{oc} of 1.09 V, a higher J_{sc} of 22.13 mA cm^2, and an elevated *FF* of 76%. The highest performance of 19.22% was achieved by 3D/LDP PSCs treated with 3F, outperforming other devices. The 3F-treated 3D/LDP devices have the following photovoltaic parameters: $V_{oc} = 1.10$ V, $J_{sc} = 22.34$ mA cm^2, and $FF = 77\%$. The observable rise in V_{oc} suggests that the trap-assisted recombination associated with defects is alleviated through the surface defect passivation and formation of the low-dimensional LDP phase at the grain boundaries of the 3D perovskite, achieved with 3F and 5F organic spacers. Additionally, the improvement in V_{oc} and *FF* is further facilitated by the acceleration of charge transport induced by surface dipoles. The higher dipole moment and lower band gap (3.26 eV) of 3F molecule, as determined by DFT, can be attributed to its superior PV performance compared to the 5F (3.54 eV) (Figure S13, Supporting Information).

Moreover, the reproducibility of PSCs devices is assessed by conducting tests on 15 cells to determine the influence of the 3F passivation on the performance of the devices, as depicted in Figure 5g. The optimal power output at the maximum power point (MPP) is achieved by the top-performing devices when operating under 40%–45% relative humidity (RH) conditions within the initial 2 min period, as illustrated in Figure 5h. The average PCE of the PSCs treated with 3F is calculated to be 18.98%, which closely matches the PCE obtained from *J–V* measurements.

The external quantum efficiency spectra (EQE) of the PSCs were measured due to their identical optical absorption spectrum as shown in Figure 5i. Given their identical optical absorption spectrum slight change has been observed in the range from 300 to 850 nm. The 2F-treated 3D/LDP hybrid device exhibits an integrated J_{sc} response of 21.03 mA cm^2, similar to the 20.94 mA cm^2 of the 3D MAPI control. The integrated J_{sc} values for the 3F and 5F modified 3D/LDP PSCs samples surpass those of the control device, with values of 21.44 and 21.23 mA cm^2, respectively. After treatment with the corresponding organic cations of the perovskite layer, the PSCs show improved efficiency in converting the absorbed light into electrical energy, which is even more evident for 3F-3D/LDP-PSCs.

Although MAPI was selected for this investigation due to its well-characterized and reproducible optoelectronic properties, which provide a reliable foundation for examining the effects of fluorinated organic spacers on performance and defect passivation, we also applied our most efficient fluorine-functionalized organic spacer, 3F, to a formamidinium lead iodide (FAPI) perovskite solar cell to demonstrate its effectiveness on other organic-inorganic perovskite structures. We successfully achieved a PCE of 22.43% for the 3F-treated FAPI, compared to a PCE of 20.95% for the control FAPI device (Figure S18, Supporting Information).

The stability of unencapsulated MAPI devices was examined in ambient air conditions (room temperature, RH (40%–45%), as depicted in **Figure 6**a. Perovskite devices treated with 2F and 3F kept 74% and 85% of their PCE following a 1000 h stability test in the dark respectively. In comparison, the PCE of the untreated 3D control device decreased to 70% of its initial value. The 5F-modified 3D/LDP PSCs exhibited superior environmental stability compared to other devices, retaining 88% of their initial PCE after 1000 h under a $\mathrm{N_2}$ atmosphere (dark), which is quite

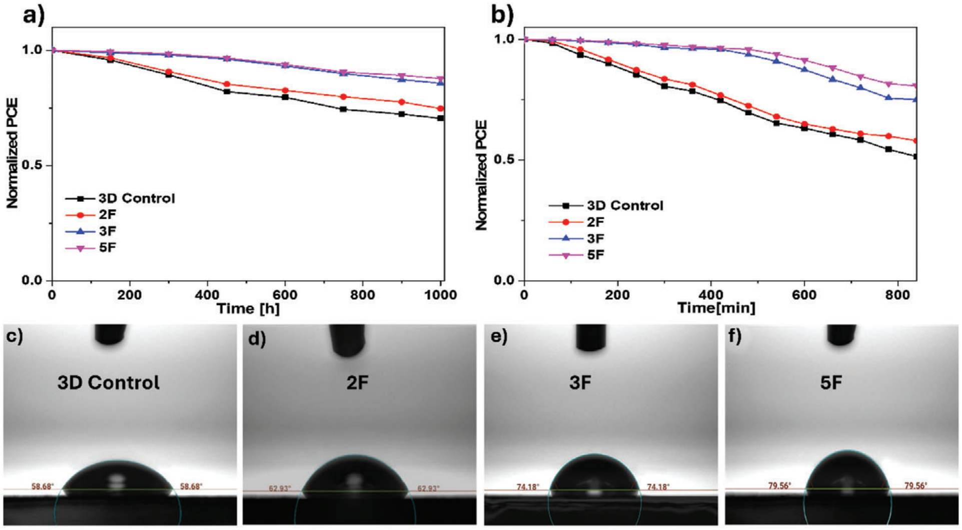

Figure 6. a) Long-term stability tests, and b) light-thermal stability curves of 3D control, 2F-3D/LDP, 3F-3D/LDP, and 5F-3D/LDP. Contact angle measurements of c) 3D MAPI control, d) 2-F, e) 3F-, and f) 5F-treated 3D/LDP perovskite film.

comparable with 3F-modified 3D/LDP PSCs (retaining 85% of their initial PCE after 1000 h). In contrast, the long-term stability of the 2F-treated perovskite films was negligible, similar to that of the 3D control device.

A light-thermal stability test was also performed on the devices by exposing them to one sun at 60 °C for 800 mins in an N_2 environment. The 3D/LDP perovskite device treated with 5F exhibited the highest light-thermal stability, maintaining 80% of its initial efficiency after 12 h of continuous light soaking, as depicted in Figure 6b, followed with 3F-treated device maintaining 75% of its initial efficiency. The PCE of 3D MAPI control and 2F-treated 3D devices reduced to 52% and 58% of their initial values, respectively. The increased stability observed in the 5F- and 3F-modified devices is attributed to several factors such as the formation of LDP phase and higher hydrophobicity, which is believed to impede ion migration and moisture infiltration, improve film quality, and reduce defects in the perovskite layer. Although the 3F molecule has higher E_b, the increased hydrophobicity of the 5F molecule provides slightly better stability, hence preserving the PCE performance. On the other hand, the lower stability in 2F treated films can be explained with the smaller binding energy and lower hydrophobicity. The rapid degradation of all devices under light-thermal stress can be attributed to the presence of the spiro-OMeTAD layer in the device architecture.[80]

To investigate the effect of the hydrophobic nature of the F atom on stability, in conjunction with the F-number of the organic spacers, the water contact angles of 3D/LDP perovskite films treated with 2F, 3F, and 5F were evaluated in comparison to the 3D MAPI control film as shown in Figure 6c–f. The 5F-modified 3D/LDP structure has the largest water contact angle, measuring ≈79°, followed with 3F-modified 3D/LDP perovskite film with contact angle of ≈74°. In contrast, the water contact angle of the 2F-modified 3D/LDP perovskite film is roughly 62°, quite close to that of the 3D MAPI control film (58°). We can deduce that LDP passivation in general has a favorable effect on the water contact angle, resulting in hydrophobic surface.

3. Conclusion

In summary, fluorine functionalized organic spacers were used to reduce defects and to fabricate mixed-dimensional 3D/LDP MAPI perovskite devices. DFT calculations showed that the 3F has the highest molecular dipole moment, followed by the 5F and 2F. When considering partial coverage, the calculated E_b of these fluorinated organic spacers on the Pb-I-terminated perovskite surface, follows an increasing trend in the sequence: 2F, 5F, and 3F. The efficacy of the passivating organic spacers and LDP was demonstrated by SSPL and TRPL studies, which suggested possible decreases in non-radiative recombination losses in treated perovskite films. CL analysis was utilized to provide a more comprehensive understanding of the emission characteristics of both the untreated and treated perovskite films. Although the 3D control displayed emission from both MAPI and excess PbI_2, the treated films that formed LDP exhibited non-emissive properties from the agglomerates and emitted a signal from the 3D MAPI. Low-dimensional phases were revealed by additional investigations using XRD, GIWAXS, and HR-TEM. These analyses also revealed changes in crystallinity, surface composition, and crystallite orientation of the passivated films.

Among these fluorinated spacers, the 3F structure showed the highest PCE. First, its higher dipole moment potentially increases the dielectric constant, reducing the Coulomb force between the exciton's electron and hole pair in the formed low-dimensional perovskite phases, thereby promoting effective charge separation. Second, the molecular structure of 3F, with its higher flexibility and trifluoromethyl unit located in the para position of the benzene ring rather than a direct attachment of F atoms to the benzene ring, gives rise to larger molecular dipole and facilitates more effective interaction between its amino group and the perovskite surface. This leads to enhanced defect passivation and, consequently, improved device performance. In addition, the presence of three F atoms in 3F provides an optimal balance that gives the perovskite layer sufficient hydrophobicity to protect it from moisture without compromising the electronic properties of the material. Therefore, 3F emerges as the most promising structure, offering an ideal combination of efficiency and stability.

Our study highlights the intricate relationship between surface morphology, molecular structure, and optoelectronic characteristics in PSCs, providing valuable insights for optimizing and improving device performance, while also emphasizing the key role of molecular design in tuning these properties through comparative analyses of these organic spacers within the same family group.

4. Experimental Section

All characterization data were derived from 3D/LDP perovskite films created using 2 mg mL^{-1} 2F, 3F, and 5F in IPA solution unless specified otherwise.

Preparation of 3D MAPI Perovskite Precursor: The 3D control solution was made by mixing PbI2 (1.68 M with a 5% excess), MAI (1.60 M), and DMSO (1.60 M) in 1 mL DMF.

Device Fabrication of 3D Control and 3D/LDP Perovskite: Glass substrates (3 × 3 cm) coated with indium-tin-oxide (ITO) underwent etching with Zn powder and 3 M HCl for 5 min. Subsequently, the ITO-coated substrates were subjected to sonication in a 2% solution of Hellmanex III cleaning agent (Sigma-Aldrich) followed by sequential immersion in double distilled water, ethanol, and isopropanol, each for a duration of 15 min. After drying the substrates with nitrogen gas, they were exposed to nitrogen plasma at 50% power for 15 min. For the 3D control and the passivated 3D/LDP MAPI perovskites, a diluted water solution containing SnO_2 nanoparticles (2.67 wt.%) was spin-coated onto FTO substrates with patterns in ambient air at 4000 rpm for 35 s. Subsequently, the coated substrates were annealed at 150 °C for 30 min. Before applying the perovskite coating, the ITO substrates coated with SnO_2 were subjected to an additional cleaning step using nitrogen plasma for 10 min. Employing the one-step "anti-solvent" method, the perovskite precursor solution of the 3D MAPI perovskite was spin-coated onto the ITO/SnO_2 layer, first at 1000 rpm for 10 s, followed by 3500 rpm for 20 s. During the final 10 s of the spin-coating step, an anti-solvent, chlorobenzene (400 µL), was introduced onto the perovskite film. Following that, the samples were annealed at 130 °C for 10 min. For the surface treatment, 2F, 3F, 5F, (2 mg) in 1 mL isopropanol solution was spin-coated onto the perovskite films at 4000 rpm for 30 s. Later, the samples were annealed at 100 °C for 5 min under N_2 atmosphere. The hole transport material (HTM) was applied through spin-coating (3000 rpm for 30 s) using a spiro-OMeTAD solution. The solution comprised 72.3 mg of spiro-OMeTAD, 35 µl of bis(trifluoromethane) sulfonimide lithium salt (LiTFSI) stock solution (270 mg LiTFSI in 1 ml acetonitrile), 30 µl of 4-tert-butylpyridine, and 1 ml of chlorobenzene. Ultimately, a thin film of Au with a thickness of 80 nm was deposited via thermal evaporation under high vacuum conditions (1×10^{-6} Pa) onto the hole transport layer. The active area was determined using a metal mask with an area of 0.0831 cm^2.

Supporting Information

Supporting Information is available from the Wiley Online Library or from the author.

Acknowledgements

Ali Semerci expresses gratitude for the financial assistance received through the Study Abroad Postgraduate Education Scholarship (YLSY), granted by the Ministry of National Education, Republic of Turkey. The authors extend their thanks to the Deutsche Forschungsgemeinschaft (DFG, German Research Foundation) for their support under Germany's Excellence Strategy-EXC 2089/1-390776260 (e-conversion). T.A. acknowledges financial support the German Research Foundation (DFG) via the Heisenberg Programme (project number AM 519/4-1) and the collaborative research center CRC 1261 (project number 286471992). S.E. acknowledges the financial assistance provided by the Slovenian Research Agency (N2-0221 and P2-0412). S.S. acknowledges support from funding by NWO START-UP (Project No. 740.018.024). S.T. acknowledges funding by NWO START-UP (Project No. 740.018.024) and VIDI (Project No. VI.Vidi.213.091) from The Netherlands. N.M., J.U.M. and N.M. thanks financial support to MCIN/AEI of Spain (projects PID2020-114653RB-I00, and TED2021-131255B-C44 funded by MCIN/AEI/10.13039/501100011033 and "(MAD2D-CM)-UCM" projects funded by Comunidad de Madrid, by the Recovery, Transformation and Resilience Plan, and by NextGenerationEU from the European Union. A.M.O. was grateful to MCIN for a "Ramon-y-Cajal" fellowship (RYC2019-027939-I).

Open access funding enabled and organized by Projekt DEAL.

Conflict of Interest

The authors declare no conflict of interest.

Data Availability Statement

The data that support the findings of this study are available in the supplementary material of this article.

Keywords

fluorinated organic spacers, mixed-dimensional perovskite, passivation, perovskite solar cell

Received: November 26, 2024
Published online:

[1] S. Akin, N. Arora, S. M. Zakeeruddin, M. Grätzel, R. H. Friend, M. I. Dar, *Adv. Energy Mater.* **2019**, *10*, 1903090.

[2] T. Yang, C. Ma, W. Cai, S. Wang, Y. Wu, J. Feng, N. Wu, H. Li, W. Huang, Z. Ding, L. Gao, S. F. Liu, K. Zhao, *Joule* **2023**, *7*, 574.

[3] W. Xiang, Z. Wang, D. J. Kubicki, W. Tress, J. Luo, D. Prochowicz, S. Akin, L. Emsley, J. Zhou, G. Dietler, M. Grätzel, A. Hagfeldt, *Joule* **2019**, *3*, 205.

[4] A. Kojima, K. Teshima, Y. Shirai, T. Miyasaka, *J. Am. Chem. Soc.* **2009**, *131*, 6050.

[5] J. Park, J. Kim, H. S. Yun, M. J. Paik, E. Noh, H. J. Mun, M. G. Kim, T. J. Shin, S. I. Seok, *Nature* **2023**, *616*, 724.

[6] H. J. Snaith, *J. Phys. Chem. Lett.* **2013**, *4*, 3623.

[7] S. D. Stranks, G. E. Eperon, G. Grancini, C. Menelaou, M. J. P. Alcocer, T. Leijtens, L. M. Herz, A. Petrozza, H. J. Snaith, *Science* **2013**, *342*, 341.

[8] W. Nie, H. Tsai, R. Asadpour, J.-C. J. C. Blancon, A. J. Neukirch, G. Gupta, J. J. J. Crochet, M. Chhowalla, S. Tretiak, M. A. Alam, H. L. H.-L. Wang, A. D. Mohite, *Science* **2015**, *347*, 522.

[9] G. E. Eperon, M. T. Horantner, H. J. Snaith, *Nat. Rev. Chem.* **2017**, *1*, 0095.

[10] S. Albrecht, M. Saliba, J. P. C. Baena, F. Lang, L. Kegelmann, M. Mews, L. Steier, A. Abate, J. Rappich, L. Korte, *Energy Environ. Sci* **2016**, *9*, 81.

[11] Z. Wang, Z. J. Shi, T. T. Li, Y. H. Chen, W. Huang, *Angew. Chem., Int. Ed.* **2017**, *56*, 1190.

[12] S. Yang, Y. Wang, P. Liu, Y.-B. Cheng, H. J. Zhao, H. G. Yang, *Nat. Energy* **2016**, *1*, 15016.

[13] P. Li, C. Liang, X.-L. Liu, F. Li, Y. Zhang, X.-T. Liu, H. Gu, X. Hu, G. Xing, X. Tao, Y. Song, *Adv. Mater.* **2019**, *31*, 1901966.
[14] Y. Rong, L. Liu, A. Mei, X. Li, H. Han, *Adv. Energy Mater.* **2015**, *5*, 1501066.
[15] B. Chen, P. N. Rudd, S. Yang, Y. Yuan, J. Huang, *Chem. Soc. Rev.* **2019**, *48*, 3842.
[16] Q. Zhou, Y. Gao, C. Cai, Z. Zhang, J. Xu, Z. Yuan, P. Gao, *Angew. Chem., Int. Ed.* **2021**, *60*, 8303.
[17] E. Akman, S. Akin, *Adv. Mater.* **2021**, *33*, 2006087.
[18] D. Shi, V. Adinolfi, R. Comin, M. Yuan, E. Alarousu, A. Buin, Y. Chen, S. Hoogland, A. Rothenberger, K. Katsiev, Y. Losovyj, X. Zhang, P. A. Dowben, O. F. Mohammed, E. H. Sargent, O. M. Bakr, *Science* **2015**, *347*, 519.
[19] Q. Wang, B. Chen, Y. Liu, Y. Deng, Y. Bai, Q. Dong, J. Huang, *Energy Environ. Sci.* **2017**, *10*, 516.
[20] S. G. Motti, D. Meggiolaro, A. J. Barker, E. Mosconi, C. A. R. Perini, J. M. Ball, M. Gadini, M. Kim, F. De Angelis, A. Petrozza, *Nat. Photon.* **2019**, *13*, 532.
[21] N. Ahn, K. Kwak, M. S. Jang, H. Yoon, B. Y. Lee, J.-K. Lee, P. V. Pikhitsa, J. Byun, M. Choi, *Nat. Commun.* **2016**, *7*, 13422.
[22] K. Kwak, E. Lim, N. Ahn, J. Heo, K. Banh, S. K. Kim, M. Choi, *Nanoscale* **2019**, *11*, 11369.
[23] C. Li, S. Tscheuschner, F. Paulus, P. E. Hopkinson, J. Kießling, A. Köhler, Y. Vaynzof, S. Huettner, *Adv. Mater.* **2016**, *28*, 2446.
[24] G. J. A. H. Wetzelaer, M. Scheepers, A. M. Sempere, C. Momblona, J. Avila, H. J. Bolink, *Adv. Mater.* **2015**, *27*, 1837.
[25] C. Eames, J. M. Frost, P. R. F. Barnes, B. C. O'Regan, A. Walsch, M. S. Islam, *Nat. Commun.* **2015**, *6*, 7497.
[26] J. M. Azpiroz, E. Mosconi, J. Bisquert, F. D. Angelis, *Energy Environ. Sci.* **2015**, *8*, 2118.
[27] N. Li, S. Tao, Y. Chen, X. Niu, C. K. Onwudinanti, C. Hu, Z. Qiu, Z. Xu, G. Zheng, L. Wang, Y. Zhang, L. Li, H. Liu, Y. Lun, J. Hong, X. Wang, Y. Liu, H. Xie, Y. Gao, Y. Bai, S. Yang, G. Brocks, Q. Chen, H. Zao, *Nat. Energy* **2019**, *4*, 408.
[28] G. Ren, W. Han, Y. Deng, W. Wu, Z. Li, J. Guo, H. Bao, C. Liu, W. Guo, *J. Mater. Chem. A* **2021**, *9*, 4589.
[29] T. Wu, Z. Qin, Y. Wang, Y. Wu, W. Chen, S. Zhang, M. Cai, S. Dai, J. Zhang, J. Liu, Z. Zou, X. Liu, H. Segawa, H. Tan, Q. Tang, J. Fang, Y. Li, L. Ding, Z. Ning, Y. Qi, Y. Zhang, L. Han, *Nano-Micro Lett.* **2021**, *13*, 152.
[30] D. Xin, S. Tie, R. Yuan, X. Zheng, J. Zhu, W. H. Zhang, *ACS Appl. Mater. Interfaces* **2019**, *11*, 44233.
[31] T. Wu, X. Li, Y. Qi, Y. Zhang, L. Han, *Chem.Sus.Chem* **2021**, *14*, 4354.
[32] Y. Liu, S. Akin, A. Hinderhofer, F. T. Eickemeyer, H. Zhu, J.-Y. Seo, J. Zhang, F. Schreiber, H. Zhang, M. Zakeeruddin, A. Hagfeldt, M. I. Dar, M. Grätzel, *Angew. Chem., Int. Ed.* **2020**, *59*, 15688.
[33] E. Khorshidi, B. Rezaei, D. Blätte, A. Buyruk, M. A. Reus, J. Hanisch, B. Böller, P. Müller-Buschbaum, T. Ameri, *Sol. RRL* **2022**, *6*, 2200023.
[34] E. Khorshidi, B. Rezaei, J. Hanisch, B. Böller, M. A. Reus, P. Müller-Buschbaum, T. Ameri, *ACS Appl. Mater. Interfaces* **2022**, *14*, 54623.
[35] L. Meng, J. You, Y. Yang, *Nat. Commun.* **2018**, *9*, 5265.
[36] A. Semerci, A. Buyruk, S. Emin, R. Hooijer, D. Kovacheva, D. Mayer, M. A. Reus, D. Blätte, M. Günther, N. F. Hartmann, S. Lotfi, J. P. Hofmann, P. MüllerBuschbaum, T. Bein, T. Ameri, *Adv. Opt. Mater.* **2023**, *11*, 2300267.
[37] A. Buyruk, D. Blätte, M. Günther, M. A. Scheel, N. F. Hartmann, M. Döblinger, A. Weis, A. Hartschuh, P. Müller-Buschbaum, T. Bein, T. Ameri, *ACS Appl. Mater. Interfaces* **2021**, *13*, 32894.
[38] J. Zhang, X. Yang, H. Deng, K. Qiao, U. Farooq, M. Ishaq, F. Yei, H. Liu, J. Tang, H. Song, *Nano-Micro Lett.* **2017**, *9*, 1.
[39] M. Shao, T. Bie, L. Yang, Y. Gao, X. Jin, F. He, N. Zheng, Y. Yu, X. Zhang, *Adv. Mater.* **2022**, *34*, 2107211.
[40] B. Saparov, D. B. Mitzi, *Chem. Rev.* **2016**, *116*, 4558.
[41] P. Chen, Y. Bai, S. Wang, M. Lyu, J. Yun, L. Wang, *Adv. Funct. Mater.* **2018**, *28*, 1706923.
[42] I. C. Smith, E. T. Hoke, D. Solis-Ibarra, M. D. McGehee, H. I. Karunadasa, *Angew. Chem., Int. Ed.* **2014**, *53*, 11232.
[43] T. D. Gangadharan, D. Ma, *Energy Environ. Sci.* **2019**, *12*, 2860.
[44] C. Katan, N. Mercier, J. Even, *Chem. Rev* **2019**, *119*, 3140.
[45] R. Hooijer, A. Weis, A. Biewald, M. T. Sirtl, J. Malburg, R. Holfeuer, S. Thamm, A. A. Y. Amin, M. Righetto, A. Hartschuh, L. M. Herz, T. Bein, *Adv. Opt. Mater.* **2022**, *10*, 2200354.
[46] J. S. Shi, Y. R. Gao, X. Gao, Y. Zhang, J. J. Zhang, X. Jing, M. Shao, *Adv. Mater.* **2019**, *31*, 1901673.
[47] Q. Zhou, Q. Xiong, Z. Zhang, J. Hu, F. Lin, L. Liang, T. Wu, X. Wang, J. Wu, B. Zhang, P. Gao, *Sol. RRL* **2020**, *4*, 2000107.
[48] F. Zhang, D. H. Kim, H. Lu, J. S. Park, B. W. Larson, J. Hu, L. Gao, C. Xiao, O. G. Reid, X. Chen, Q. Zhao, P. F. Ndione, J. J. Berry, W. You, A. Walsh, M. C. Beard, K. Zhu, *J. Am. Chem. Soc.* **2019**, *141*, 5972.
[49] Y. Wei, P. Audebert, L. Galmiche, J. S. Lauret, E. Deleporte, *J. Phys. D. Appl. Phys.* **2013**, *46*, 135105.
[50] Y. Liu, S. Akin, L. Pan, R. Uchida, N. Arora, J. V. Milić, A. Hinderhofer, F. Schreiber, A. R. Uhl, S. M. Zakeeruddin, A. Hagfeldt, M. I. Dar, M. Grätzel, *Sci. Adv.* **2019**, *5*, eaaw2543.
[51] J. Zhou, M. Li, S. Wang, L. Tan, Y. Liu, C. Jiang, X. Zhao, L. Ding, C. Yi, *Nano Energy* **2022**, *95*, 107036.
[52] H. Zhu, Y. Ren, L. Pan, O. Ouellette, F. T. Eickemeyer, Y. Wu, X. Li, S. Wang, H. Liu, X. Dong, S. M. Zakeeruddin, Y. Liu, A. Hagfeldt, M. Grätzel, *J. Am. Chem. Soc.* **2021**, *143*, 3231.
[53] D. Li, Z. Xing, L. Huang, X. Meng, X. Hu, T. Hu, Y. Chen, *Adv. Mater* **2021**, *33*, 2101823.
[54] X. Lai, W. Li, X. Gu, H. Chen, Y. Zhang, G. Li, R. Zhang, D. Fan, F. He, N. Zheng, J. Yu, R. Chen, A. K. K. Kyaw, X. W. Sun, *J. Chem. Eng.* **2022**, *427*, 130949.
[55] W. Shi, H. Ye, *J. Phys. Chem. Lett.* **2021**, *12*, 4052.
[56] T. Zhou, H. Lai, T. Liu, D. Lu, X. Wan, X. Zhang, Y. Liu, Y. Chen, *Adv. Mater.* **2019**, *31*, 1901242.
[57] A. Amat, E. Mosconi, E. Ronca, C. Quarti, P. Umari, M. K. Nazeeruddin, M. Grätzel, F. De Angelis, *Nano Lett.* **2014**, *14*, 3608.
[58] J. W. Xiao, L. Liu, D. Zhang, N. De Marco, J. W. Lee, O. Lin, Q. Chen, Y. Yang, *Adv. Energy Mater.* **2017**, *7*, 1700491.
[59] Y. Dong, D. Lu, Z. Xu, H. Lai, Y. Liu, *Adv. Energy Mater.* **2020**, *10*, 2000694.
[60] Q. Li, Y. Dong, G. Lv, T. Liu, D. Lu, N. Zheng, X. Dong, Z. Xu, Z. Xie, Y. Liu, *ACS Energy Lett.* **2021**, *6*, 2072.
[61] J. S. Shi, Y. R. Gao, X. Gao, Y. Zhang, J. J. Zhang, X. Jing, M. Shao, *Adv. Mater.* **2019**, *31*, 1901673.
[62] J. Hu, I. W. H. Oswald, H. Hu, S. J. Stuard, M. M. Nahid, L. Yan, Z. Chen, H. Ade, J. R. Neilson, W. You, *Acs Mater. Lett.* **2019**, *1*, 171.
[63] Z. Ren, X. Xiao, R. Ma, H. Lin, K. Wang, X. W. Sun, W. C. H. Choy, *Adv. Funct. Mater.* **2019**, *29*, 1905339.
[64] C. Xiao, Z. Li, H. Guthrey, J. Moseley, Y. Yang, S. Wozny, H. Moutinho, B. To, J. J. Berry, B. Gorman, *J. Phys. Chem. C* **2015**, *119*, 26904.
[65] Q. Li, Y. Dong, G. Lv, T. Liu, D. Lu, N. Zheng, X. Dong, Z. Xu, Z. Xie, Y. Liu, *ACS Energy Lett.* **2021**, *6*, 2072.
[66] R. Lin, J. Xu, M. Wei, Y. Wang, Z. Qin, Z. Liu, J. Wu, K. Xiao, B. Chen, S. M. Park, G. Chen, H. R. Atapattu, K. R. Graham, J. Xu, J. Zhu, L. Li, C. Zhang, E. H. Sargent, H. Tan, *Nature* **2022**, *603*, 73.
[67] P. Chen, Y. Bai, S. Wang, M. Lyu, J. H. Yun, L. Wang, *Adv. Funct. Mater.* **2018**, *28*, 1706923.
[68] J. Shi, Y. Gao, X. Gao, Y. Zhang, J. Zhang, X. Jing, M. Shao, *Adv. Mater.* **2019**, *31*, 1901673.
[69] T. Liu, J. Guo, D. Lu, Z. Xu, Q. Fu, N. Zheng, Z. Xie, X. Wan, X. Zhang, Y. Liu, Y. Chen, *ACS Nano* **2021**, *15*, 7811.
[70] W. S. Yang, B. W. Park, E. H. Jung, N. J. Jeon, Y. C. Kim, D. U. Lee, S. S. Shin, J. Seo, E. K. Kim, J. H. Noh, S. il Seok, *Science* **2017**, *356*, 1376.

[71] M. H. Li, H. H. Yeh, Y. H. Chiang, U. S. Jeng, C. J. Su, H. W. Shiu, Y. J. Hsu, N. Kosugi, T. Ohigashi, Y. A. Chen, P. S. Shen, P. Chen, T. F. Guo, *Adv. Mater.* **2018**, *30*, 1801401.

[72] J. W. Lee, Z. Dai, T. H. Han, C. Choi, S. Y. Chang, S. J. Lee, N. De Marco, H. Zhao, P. Sun, Y. Huang, Y. Yang, *Nat. Commun.* **2018**, *9*, 3021.

[73] W. J. Wei, X. X. Jiang, L. Y. Dong, W. W. Liu, X. B. Han, Y. Qin, K. Li, W. Li, Z. S. Lin, X. H. Bu, P. X. Lu, *J. Am. Chem. Soc.* **2019**, *141*, 9134.

[74] Q. Li, Y. Dong, G. Lv, T. Liu, D. Lu, N. Zheng, X. Dong, Z. Xu, Z. Xie, Y. Liu, *ACS Energy Lett.* **2021**, *6*, 2072.

[75] J. Byeon, S. H. Cho, J. J. Jang, C. Katan, J. Even, J. Xi, M. Choi, Y. S. Lee, *ACS Appl. Mater. Interfaces* **2023**, *15*, 27853.

[76] H. N. Si, Q. L. Liao, Z. Kang, Y. Ou, J. J. Meng, Y. C. Liu, Z. Zhang, Y. Zhang, *Adv. Funct. Mater.* **2017**, *27*, 1701804.

[77] T. J. Jacobsson, J. P. Correa-Baena, E. Halvani Anaraki, B. Philippe, S. D. Stranks, M. E. F. Bouduban, W. Tress, K. Schenk, J. Teuscher, J. E. Moser, H. Rensmo, A. Hagfeldt, *J. Am. Chem. Soc.* **2016**, *138*, 10331.

[78] D. Q. Bi, W. Tress, M. I. Dar, P. Gao, J. Luo, C. Renevier, K. Schenk, A. Abate, F. Gıordano, J.-P. C. Baena, J.-D. Decoppet, S. M. Zakeeruddin, M. Grätzel, A. Hagfeldt, *Sci. Adv.* **2016**, *2*, 1501170.

[79] X. Zhang, X. Ren, B. Liu, R. Munir, X. Zhu, D. Yang, J. Li, Y. Liu, D.-M. Smilgies, R. Li, Z. Yang, T. Niu, X. Wang, A. Amassian, K. Zhao, S. F. Liu, *Energy Environ. Sci.* **2017**, *10*, 2095.

[80] S. Akin, M. Bauer, D. Hertel, K. Meerholz, S. M. Zakeeruddin, M. Grätzel, P. Bäuerle, M. I. Dar, *Adv. Funct. Mater.* **2022**, *32*, 2205729.